

Microscopic description of the torque acting on fission fragments

Guillaume Scamps **Department of Physics, University of Washington, Seattle, Washington 98195-1560, USA*

(Received 21 September 2022; accepted 9 November 2022; published 30 November 2022)

When two fragments are created in a fission decay, any torque due to nuclear and Coulomb interaction can change the fragment's angular momentum. This paper explores the character and magnitude of the angular momentum as a function of the initial conditions around the scission point using the time-dependent Hartree-Fock theory. To understand the torque acting on the fragments, the Frozen Hartree-Fock method is also used to determine the collective potential at scission. Two ^{240}Pu fission channels ($^{132}\text{Sn} + ^{108}\text{Ru}$ and $^{144}\text{Ba} + ^{96}\text{Sr}$) are studied. These two channels cover different shapes (spherical, quadrupole, and octupole deformation) of the fragments. It is found that the angular momentum generated by the Coulomb interaction after fission is mainly collective, while this is not the case for the angular momentum generated at scission. The competition between rotational modes (bending, wriggling, and twisting) is discussed and shows that the angular momentum is generated mainly perpendicular to the fission axis.

DOI: [10.1103/PhysRevC.106.054614](https://doi.org/10.1103/PhysRevC.106.054614)

I. INTRODUCTION

The generation of angular momentum in fission has several mechanisms at different stages of the fission process. One source is the fluctuations that build up during the shape evolution between the initial configuration and the scission [1–4]. At the scission point, the fragments are deformed and tend to be aligned with the fission axis. Such polarization of the fragment creates an angular momentum [5,6] due to the uncertainty principle [7]. Once the fragments are separated, the Coulomb force can create a torque leading to an additional angular momentum [8–10]. This last effect is found to have large theoretical uncertainties [10–12].

Recently, a new method has been proposed to extract the angular distribution microscopically in static [13,14] and dynamic [15,16] density functional theory. While the projection is a powerful tool to extract exactly the distribution of a discrete observable in a quantum N -body wave function, the calculation still suffers from limitations due to the theory producing that state. In a mean-field dynamic calculation, the fluctuations of the mean field are not taken into account, which prevents the self-consistent description of the Coulomb-induced rotation. To overcome that limitation would require the use of a beyond mean-field method such as a stochastic treatment [17,18] of the fission.

In this work, it is assumed that fluctuations built during the descent of the system from the saddle to the scission lead to a pair of fragments at a given deformation, distance, and orientation at scission. The goal of the present calculation is to investigate the last stage of fission using the frozen Hartree-Fock (FHF) method [19,20] (equivalent to the sudden approximation [21–24]) and the time-dependent Hartree-Fock (TDHF) method [25,26] to understand the mechanism responsible to the generation of angular momenta during and after

the scission. Nevertheless, the present paper will not discuss the source and the amplitude of the initial fluctuations of the orientation angle of the fragments. This limits the conclusion of the present work to only qualitative results.

II. METHOD

To understand the rotation during the scission, different TDHF trajectories are computed for a variety of scission configurations. In a three-dimensional Cartesian grid discretized with $N_x = N_y = 30$, $N_z = 130$ and a mesh spacing $dx = 0.8$ fm, two fragments are placed at a distance D between their center of mass on the z axis. The heavy (H) and light (L) fragments are rotated to form an angle θ_H (θ_L) with the z axis. The rotation is performed on the y axis such that the principal axis of deformation of the fragments stays in the x - z plane. When both fragments are deformed an additional rotation of an angle φ is performed for the light fragment around the fission axis (z axis). Combinations of θ_H , θ_L , and φ cover all the possible relative orientations of the fragments. The wave function of the fragments can overlap at short distances D , in which case the Gram-Schmidt antisymmetrization procedure is used before performing the TDHF evolution. The initial wave function is obtained from a static Hartree-Fock calculation; then the initial velocity and angular momentum of the fragments start at zero. The TDHF dynamics and static calculations are obtained using the SLy4D functional [27] with a simplified version of the LISE code [28] without pairing. The time evolution is done using the Runge-Kutta method at the order 4 with a time step $\Delta t = 0.3$ fm/c.

Two final-state channels are studied with different deformations to disentangle the different mechanisms. The first is the $^{132}\text{Sn} + ^{108}\text{Ru}$ channel where the heavy fragment is taken as spherical and the light one is superdeformed. The other is the $^{144}\text{Ba} + ^{96}\text{Sr}$ for which the heavy fragment has an octupole deformation and the light one has a strong quadrupole

*gscamps@uw.edu

TABLE I. Quadrupole and octupole deformation parameters and rigid moment of inertia of the four nuclei considered in this study. The rigid moment of inertia is obtained on an axis perpendicular to the main deformation axis of the nucleus. The excitation energy E^* of the deformed state is also shown. Note that the deformed wave functions are in the ground state except ^{108}Ru , which is in a local HF minimum.

Nuc.	β_2	β_3	E^* [MeV]	I_{Rigid} [\hbar^2/MeV]
^{132}Sn	0.	0.	0	50.0
^{144}Ba	0.22	0.16	0	63.1
^{108}Ru	0.82	0.	3.5	51.4
^{96}Sr	0.53	0.	0	37.1

deformation. For each system, two cases are discussed, one at a large distance where only the Coulomb interaction makes the fission fragments interact with each other, and one at a smaller distance for which the fragments touch and form a neck that supports a nuclear interaction between the fragments.

The initial Hartree-Fock (HF) wave functions are obtained with the SKY3D code [29]. The SKY3D code has been slightly modified to induce an initial octupole deformation at the beginning of the HF process. By choosing carefully the initial deformation for these systems, the HF calculation converges to the final deformations shown on Table I. The values obtained are comparable to the ones that emerge in microscopic models for the asymmetric fission of the actinide in typical static [14,30,31] and dynamical calculations [32–35], i.e., a spherical heavy fragment or one with an octupole deformation, and a light fragment with a large quadrupole deformation.

The deformations parameters are computed as

$$\beta_L = \frac{4\pi}{3A(r_0 A^{1/3})^L} Q_{l0}, \quad (1)$$

$$Q_{20} = \sqrt{\frac{5}{16\pi}} \int d^3r \rho(\mathbf{r})(2z^2 - x^2 - y^2), \quad (2)$$

$$Q_{30} = \sqrt{\frac{7}{16\pi}} \int d^3r \rho(\mathbf{r})[2z^3 - 3z(x^2 + y^2)], \quad (3)$$

with $r_0 = 1.2$ fm.

III. RESULTS

A. $^{240}\text{Pu} \rightarrow ^{132}\text{Sn} + ^{108}\text{Ru}$

1. Large distance effect of the Coulomb repulsion

Figure 1 shows the dynamics of the postscission evolution of the fragments $^{132}\text{Sn} + ^{108}\text{Ru}$ starting at a distance $D = 17$ fm and a light fragment rotated by an angle of 25° [see Fig. 1(a)]. The Coulomb repulsion produces a torque on the light fragment that causes it to rotate, as can be seen in Figs. 1(b) and 1(c). In Figs. 1(b) and 1(c), the local angular

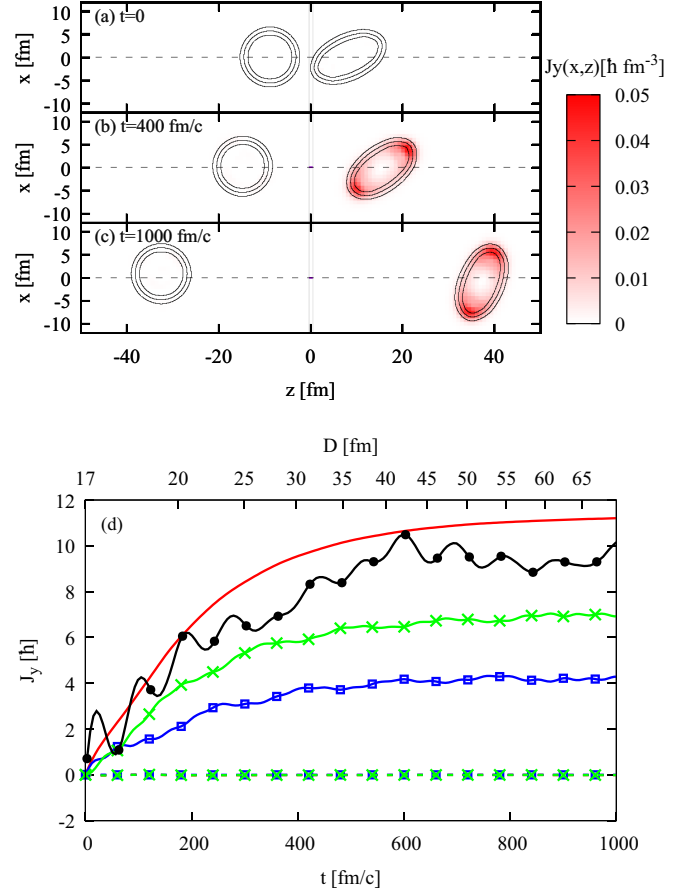


FIG. 1. Evolution of fissioning fragment ^{132}Sn (left) + ^{108}Ru (right) initially at a distance $D = 17$ fm. The ^{108}Ru fragment is initially rotated by an angle $\theta = 25^\circ$. (a)–(c) show the contour line at densities $\rho = 0.03, 0.08$, and 0.13 fm^{-3} at the time $t = (0, 400, 1000)$ fm/c. The angular momentum density [the y component of Eq. (4)] is shown by the color scale. (d) The evolution of the angular momentum as a function of time and distance D is shown for the heavy fragment (dashed line) and the light fragment (continuous line). The proton, neutron, and total angular momentum are shown with blue squares, green crosses, and red lines, respectively. The black line with bullets shows the angular momentum computed with Eq. (5). In the present case, all the components of the angular momentum are close to zero for the heavy fragments.

momentum,

$$\mathbf{J}(\mathbf{r}) = \hbar \sum_i \langle \Phi_i(\mathbf{r}) | ((\hat{\mathbf{r}} - \mathbf{r}_{\text{cm}}) \times (\hat{\mathbf{p}} - \mathbf{p}_{\text{cm}}) + \hat{\mathbf{s}}) \cdot \hat{\mathbf{S}}_i | \Phi_i(\mathbf{r}) \rangle, \quad (4)$$

is shown for the y direction in the $y = 0$ plane. \mathbf{r}_{cm} and \mathbf{p}_{cm} are, respectively, the position and momentum of the center of mass of the fragments. $\hat{\mathbf{S}}_i$ is the projector operator on the half-space containing the fragment F . The division between the fragments is chosen as the plane $z = 0$. Different prescriptions for the position of the plane of division would lead to small changes of the angular momentum when the fragments touch each other but give the same results when they are well separated. In Fig. 1(d), the integral of $J_y(\mathbf{r})$ in the whole space is shown as a function of time for protons, neutrons, and

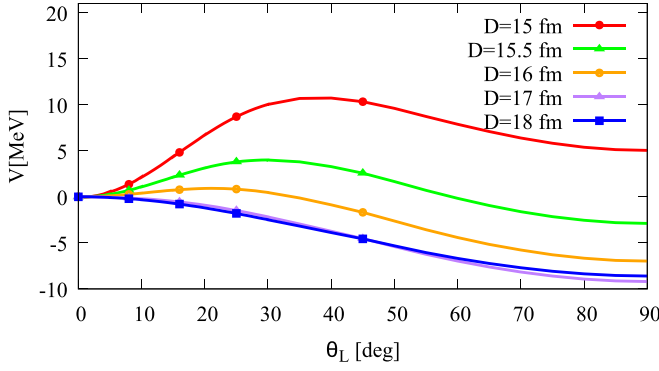


FIG. 2. Frozen Hartree-Fock potential as a function of the orientation angle θ_L of the light fragment and the distance D between the center of mass of the ^{132}Sn and ^{108}Ru fragments.

the sum of the two. The total angular momentum can also be extracted from the angular velocity $\dot{\theta}$ assuming that the moment of inertia I_y is that of a rigid body,

$$J_y^{\text{Rigid}}(t) = I_y^{\text{Rigid}}(t)\dot{\theta} \quad (5)$$

with $\theta(t)$ the angle between the principal axis of deformation of the fragment and the z axis. As expected the spherical heavy fragment does not rotate and then has zero intrinsic angular momentum. For the light fragment, the initial tilted orientation let the Coulomb potential create a torque in the fragment that tends to increase the θ_L angle resulting at a large distance by a value of the intrinsic spin of $11\hbar$. This value is large and probably exaggerated in the present calculation due to the assumption of a large initial angle θ_L . As can be seen in Fig. 3 the final angular momentum depends strongly on the initial angle. Obviously, the torque disappears for initial values of $\theta_L = 0$ and 90° .

The potential responsible for the torque is shown in Fig. 2. The potential is computed with the frozen Hartree-Fock method [19,20]. With that method, both fragments are placed in the same lattice and the energy is computed from the sum of the densities of the two fragments. Note that in the present case, the Gram-Schmidt antisymmetrization procedure is not applied. The antisymmetrization would modify strongly the shape of the potential at short distances making it incompatible with the corresponding dynamical results as shown in Appendix. A better method to obtain the potential would be to use the density-constrained Hartree-Fock theory [19] but it has been found too demanding in terms of calculations and complicated to converge in the present case.

The potential is defined to be 0 for the angle $\theta_L = 0$,

$$V(\theta_L, D) = E_{\text{FHF}}(\theta_L, D) - E_{\text{FHF}}(\theta_L = 0, D). \quad (6)$$

This frozen potential for $D > 17$ fm shows that the $\theta_L = 90^\circ$ configuration is more stable than the 0° one. Immediately after the scission, the difference of energy is about 10 MeV. As the fragments move apart, $V(\theta_L, D)$ decreases as D^{-3} , as expected for a quadrupole Coulomb interaction.

It should be noted that the TDHF calculation preserves the expectation value of the total angular momentum. It is initially zero since no boost is applied. The heavy fragment has no

final angular momentum, and the orbital angular momentum \bar{L} is equal to $-\bar{J}_L$. This angular momentum results in a small velocity for the fragments in the x direction, positive for the light fragment and negative for the heavy in the present case. The resulting small shift of position of the fragment in the x direction is visible in Fig. 1(c). In practice, due to the numerical implementation, the total angular momentum deviates less than $0.1\hbar$ from 0.

It is interesting to compare the TDHF results with the simpler model of Ref. [12]. In that model, damping of the quadrupole deformation plays an important role, which reduces the final angular momentum created by the Coulomb from about $5\hbar$ to $2\hbar$. In the present calculation, no damped vibration of the quadrupole deformation is found. The large quadrupole deformation persists throughout the Coulomb separation phase.

In Fig. 1, the total J_y and J_y^{rigid} present two different behaviors. The first one increases continuously from 0 to a final value of $11.3\hbar$ while the rigid calculation oscillates and saturates at a value around $9.5\hbar$. The oscillations have been found to be due to the excitation of the low-energy quadrupole vibration that squeezes the nuclei in the z axis and so changes the orientation of the principal axis. The difference between the two asymptotic values is interpreted as follows: Some parts of the angular momentum are stored in an internal motion of the nucleon inside the mean field and do not lead to a contribution to the collective rotation of the fragment. A more pronounced effect of this noncollective rotation will be presented in the following case.

2. Short distance effect of the nuclear interaction

The impact of the nucleus-nucleus potential is visible in Fig. 4 for which the fragments are initially placed at a center-of-mass separation $D = 15$ fm. The fragments not only feel the torque due to the Coulomb repulsion but also a stronger torque in the opposite direction that is due to the attractive nucleus-nucleus interaction. The torque can be deduced from the potential of Fig. 2 at a short distance. The complex dynamics of the two fragments result in a bending mode¹ with an angular momentum of $3.7\hbar$ for the heavy fragment and $-8.6\hbar$ for the light. The light fragment keeps its large deformation during the process and a major part of the angular momentum is collective. Nevertheless, the excitation of a large variety of modes due to the neck breaking complicates the analysis of the angular momentum generated in the fragments. Indeed, comparison with Fig. 1 shows that a larger part of the angular momentum is internal to the nuclei: (i) in Fig. 4(c) the angular momentum is not evenly spread on the surface of nuclei; (ii) the rigid angular momentum has larger oscillations; and (iii) protons and neutrons exchange continuously about $1\hbar$ of angular momentum, which may be due to the excitation of a scissor mode.

As in the Coulomb case, the results depend on the initial angle, as can be seen in Fig. 3. The top panel of that

¹The angular momentum of each fragment are in opposite direction and perpendicular to the fission axis.

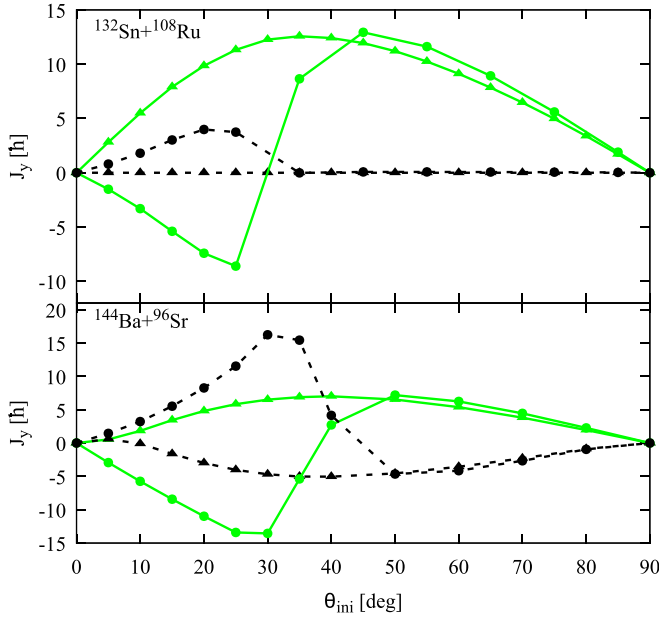


FIG. 3. Final angular momentum in the y axis for the heavy fragment (black dashed line) and the light fragment (green solid line) as a function of the initial angle θ_L starting at a distance $D = 17$ fm (triangles) and $D = 15$ fm (bullet) in the case of the fission output $^{132}\text{Sn} + ^{108}\text{Ru}$ (top) and $^{144}\text{Ba} + ^{96}\text{Sr}$ (bottom).

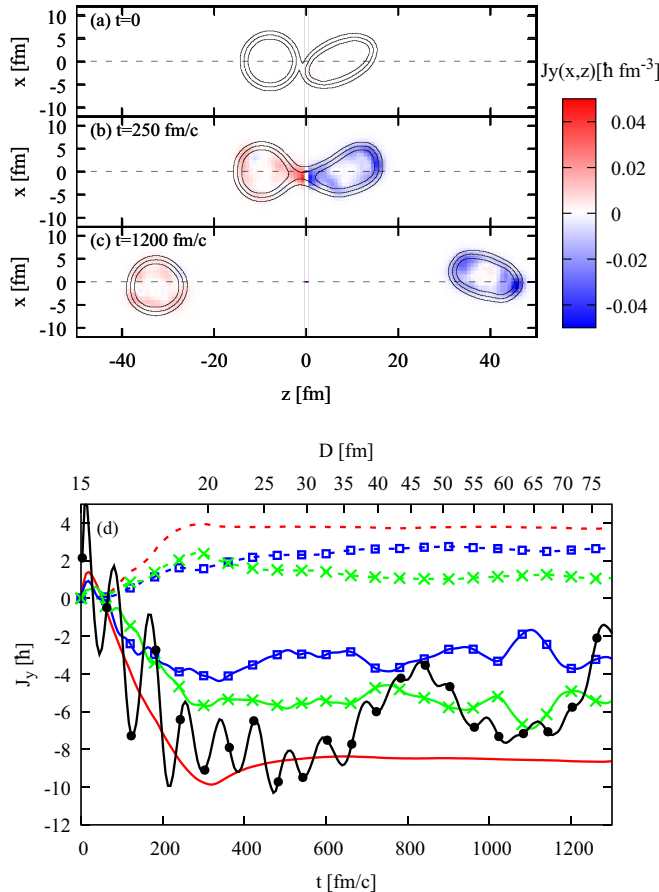


FIG. 4. Same as Fig. 1 for an initial distance $D = 15$ fm and $\theta_L = 25^\circ$.

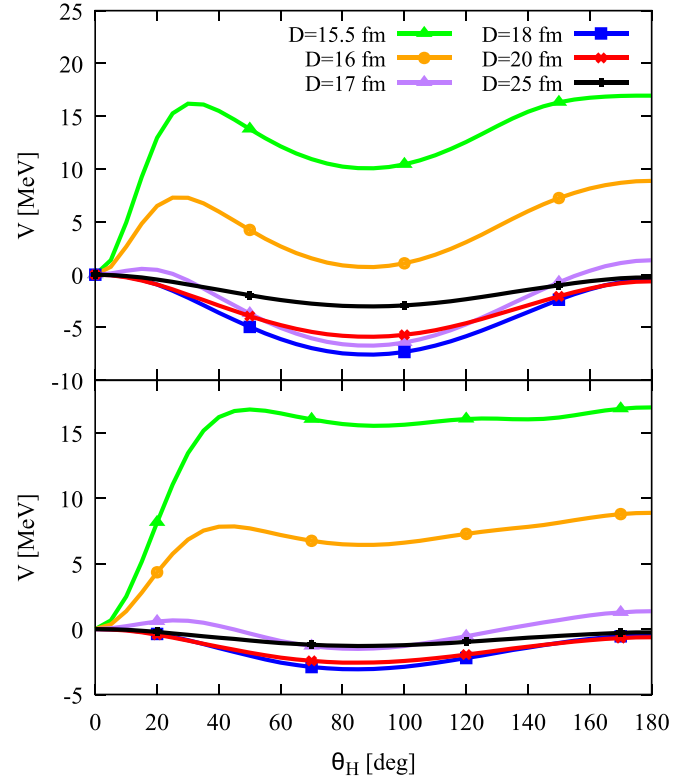


FIG. 5. Frozen Hartree-Fock potential as a function of the orientation angle θ_H of the heavy fragment and the distance D between the center of mass of the ^{144}Ba and ^{96}Sr fragments with $\theta_L = -\theta_H$ (top) and $\theta_L = 0$ (bottom). All of the calculations are obtained with $\varphi = 0$.

figure shows that the generated angular momentum depends almost linearly on the initial angle until an angle of about 30° for which the fragment stop touching each other and so the Coulomb torque dominate leading to a situation similar to the $D = 17$ fm case.

The rotation of the heavy fragment is even more peculiar. The initial fragment is spherical, but the neck and the transfer of a small number of nucleons (1.5 neutrons and 0.8 protons from the light to the heavy fragment) lead to a small deformation that breaks the spherical symmetry. Then, the rapid movement of the neck along the x axis just before scission induces a rotation of the heavy fragment. The quasiparticle fragment has a final angular momentum of $3.7 \hbar$. Surprisingly, protons contribute the most to angular momentum, although their rigid moment of inertia is lower. A slow transfer of angular momentum from neutrons to protons was also observed. No explanation for this effect has been found. The angular momentum assuming a rigid fragment is not shown in Fig. 4 because shape fluctuations cause the main axis to oscillate with large amplitudes, resulting in nonphysical rigid angular momentum.

B. $^{240}\text{Pu} \rightarrow ^{144}\text{Ba} + ^{96}\text{Sr}$

1. Dependence of the potential with the orientation

With both fragments deformed, the nucleus-nucleus potential depends on three angles, the two angles θ_H , θ_L , and the

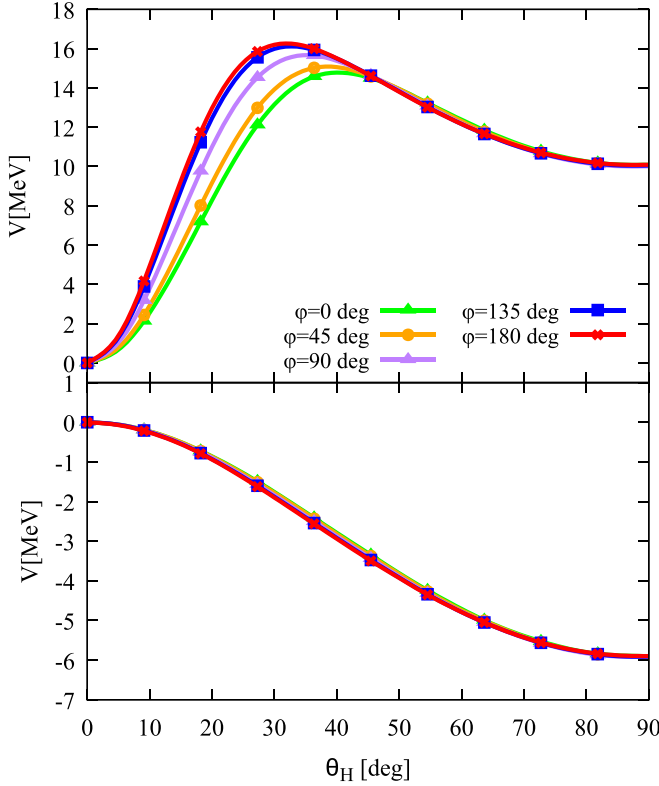


FIG. 6. Frozen Hartree-Fock potential as a function of the orientation angle θ_H of the heavy fragment taking $\theta_L = -\theta_H$ and several values of the azimuthal angle φ between the ^{144}Ba and ^{96}Sr fragments. The separation distance is $D = 15.5$ fm (20 fm) for the top (bottom) panel respectively.

azimuthal angle φ . The potential is shown in Fig. 5 for two cases as a function of the heavy fragment orientation angle. In the first case, both fragments are rotated with opposite angles, while in the second case only the heavy fragment is rotated. In both cases, it is interesting to note the strong effect of the octupole asymmetry of the heavy fragment. It induces a large difference of the potentials at angle $\theta_H = 0$ and $\theta_H = 180^\circ$, while in the case of pure quadrupole deformation the potential is symmetric with respect to the angle $\theta = 90^\circ$. At larger distances, the Coulomb potential is mostly unaffected by the octupole deformation.

At short distances, the potential is strongly dependent on both θ_H and θ_L and can not be separated into two independent contributions of each fragment. Furthermore, the azimuthal angle φ can change the energy up to a few MeV as can be seen in Fig. 6. However, note that the dependence on φ is significant only at the shorter separation and only for a limited range of $\theta_H (= -\theta_L)$.

At large distances, where only the Coulomb interaction plays a role, the azimuthal angle φ does not affect much the energy of the system (see bottom panel of Fig. 6). Similarly, the energy of the system can be well described by the independent contribution of the two fragments, i.e., the deviation,

$$|V(\theta_H, \theta_L) - V(\theta_H, 0) - V(0, \theta_L)| \quad (7)$$

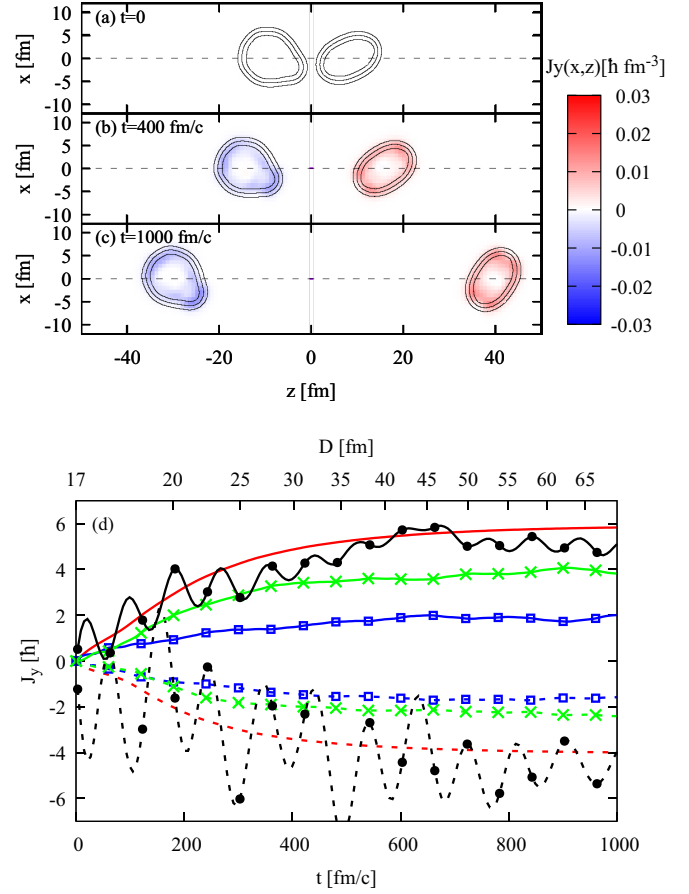


FIG. 7. Same as Fig. 4 for the fission fragments $^{144}\text{Ba} + ^{96}\text{Sr}$ with $D = 17$ fm, $\theta_H = -\theta_L = 25^\circ$ and $\varphi = 0$.

never exceed 0.35 MeV while $V(\theta_H, \theta_L)$ vary up to 6 MeV for $D = 20$ fm. With

$$V(\theta_H, \theta_L) = E_{FHF}(\theta_H, \theta_L) - E_{FHF}(0, 0). \quad (8)$$

Then, the torque due to the Coulomb interaction acting on each fragment is mainly independent of the orientation of the other fragment.

2. Large distance effect of the Coulomb repulsion

The time-dependent evolution of the system $^{144}\text{Ba} + ^{96}\text{Sr}$ at a distance $D = 17$ fm with $\theta_H = -\theta_L = 25^\circ$ is shown in Fig. 7. The evolution of the light ^{96}Sr fragment is similar to the one of the ^{108}Ru in Fig. 1: A generation of angular momentum mainly collective. Comparing the top and bottom panels of Fig. 3, it can be seen that the final angular momentum is less in ^{96}Sr than in ^{108}Ru by about a factor of two. This may be attributed to the lower value of the quadrupole moment in ^{96}Sr . The heavy fragment shows also a rotation with a final value of the angular momenta of 4 \hbar due to the small quadrupole and octupole deformation.

In Ref. [36], it is argued that the postscission Coulomb-induced rotation would be dependent on the product of the charge of the fragments $Z_1 Z_2$, which is incompatible with the experimental data. Nevertheless, the comparison

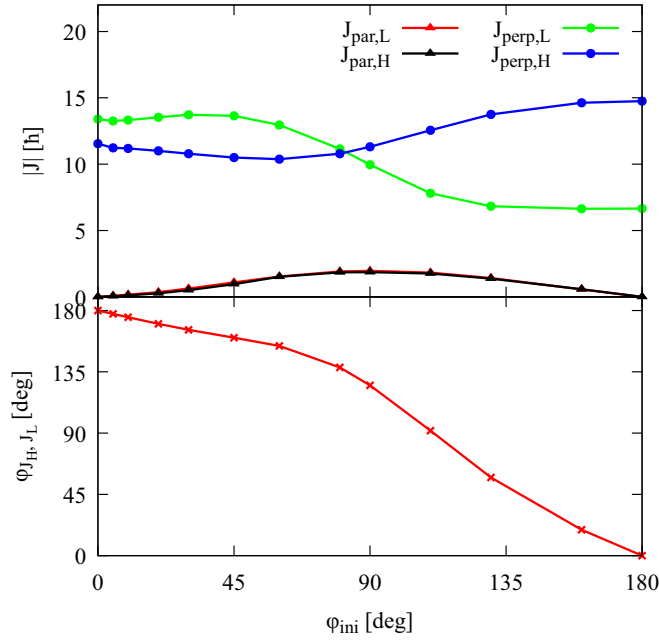


FIG. 8. Angular momentum in the direction perpendicular and parallel to the motion of the heavy and light fragment (top). The bottom panel shows the angle between the two angular momenta φ_{J_H, J_L} as a function of the initial azimuthal angle φ . Both panels are showing results obtained for the $^{144}\text{Ba} + ^{96}\text{Sr}$ at initial distance $D = 15$ fm and $\theta_H = -\theta_L = 25^\circ$.

of the two fission outputs $^{132}\text{Sn} + ^{108}\text{Ru}$ ($Z_1 Z_2 = 2200$) and $^{144}\text{Ba} + ^{96}\text{Sr}$ ($Z_1 Z_2 = 2128$) in Fig. 3 show that the main parameters that influence the generation of angular momentum by Coulomb are (i) the initial angle of the fragments and (ii) the deformation parameters. It is difficult to estimate how the initial angle would depend on the asymmetry of the fission but it is expected that the quadrupole would have a sawtooth shape as a function of the asymmetry, which would make it compatible with the experimental data of Ref. [36].

3. Short distance, parallel, and perpendicular component of the angular momentum

The dependence of the potential on the angle φ shown in Fig. 6 is inducing a twisting² rotational mode if the initial φ angle is different from 0 or 180° . This effect is shown in Fig. 8, where calculations are done as a function of the azimuthal angle at initial distance $D = 15$ fm and $\theta_H = -\theta_L = 25^\circ$. For each fragment, the angular momentum is decomposed into two components, one parallel to the motion of the fragment and one perpendicular to it. The parallel component describes the twisting component of the rotation. A maximum value of $2.0 \hbar$ is obtained for $\varphi = 90^\circ$. This is much smaller than the perpendicular component with an average of around $10 \hbar$. The smaller angular momentum in the twisting mode

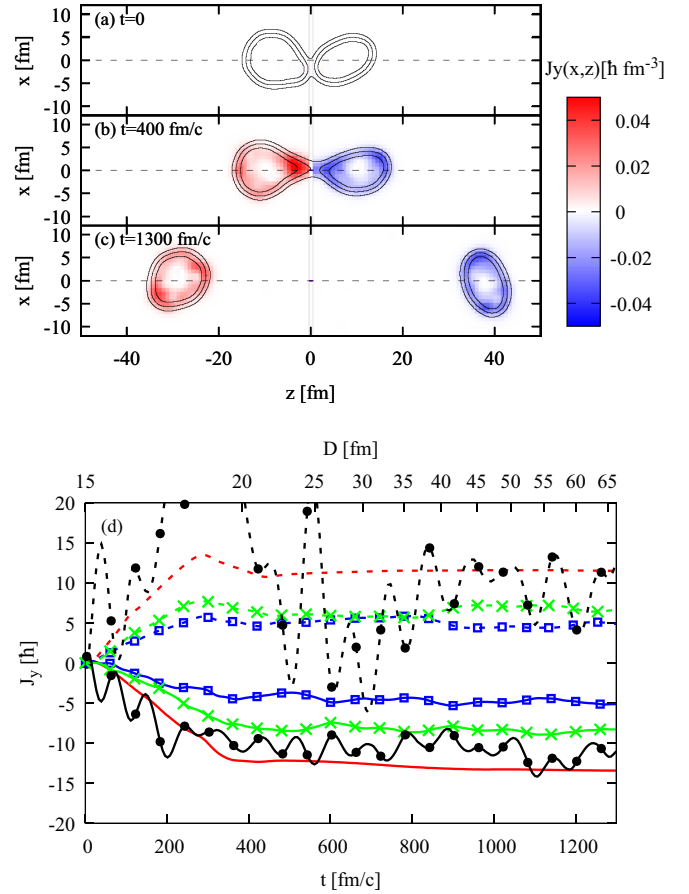


FIG. 9. Same as Fig. 7 for the system $^{144}\text{Ba} + ^{96}\text{Sr}$ with $D = 15$ fm, $\theta_H = -\theta_L = 25^\circ$ and $\varphi = 0$.

is due to: (i) the gradient of the nuclear potential is smaller in the φ direction than in θ as shown in Fig. 6 and (ii) the Coulomb potential very weakly contributes to the twisting mode after scission. The parallel component is purely a twisting mode (the perpendicular components of the fragment have the same norm, oriented in opposite directions) since the total angular momentum about the fission axis is conserved.

The angle between the angular momentum φ_{J_H, J_L} is shown on the bottom panel of Fig. 8. It shows that the rotational mode is purely a bending mode for $\varphi = 0^\circ$ to a purely wriggling³ mode for $\varphi = 180^\circ$. Between these two values, the function of φ_{J_H, J_L} is not linear but tend to stay closer to the 180° value. In a statistical approach, assuming a constant distribution of angle φ between 0 – 180° would lead to a distribution of φ_{J_H, J_L} populating more the final states with angle $\varphi_{J_H, J_L} > 90^\circ$. This result is in qualitative agreement with the results found in Refs. [16,37].

In Fig. 9, similarly to the $^{132}\text{Sn} + ^{108}\text{Ru}$ case, the strong nuclear interaction creates a large torque leading to a noncollective rotation of both fragments. They gain the dom-

²The angular momentum of each fragment are in opposite direction and parallel to the fission axis.

³The angular momenta of the fragments are in the same directions and perpendicular to the fission axis.

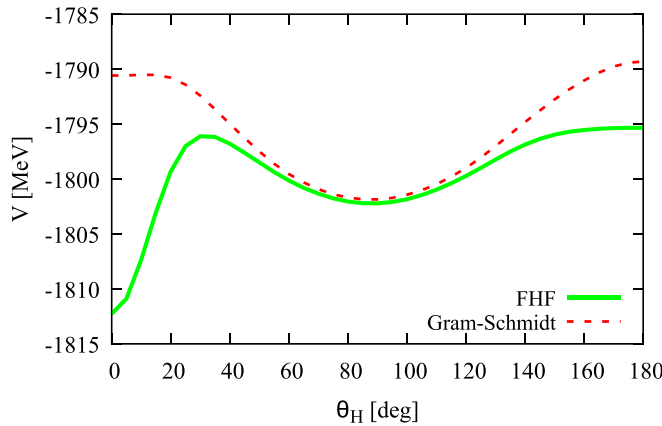


FIG. 10. Energy of the $^{144}\text{Ba} + ^{96}\text{Sr}$ at a distance $D = 15.5$ fm as a function of the orientation angle of the ^{144}Ba with and without the orthogonalization of the wave functions.

inant part of their angular momentum before the scission (around $t = 400$ fm/c). The Coulomb potential only contributes to a small additional angular momentum for the light fragment.

IV. CONCLUSION

Using the DFT-TDDFT framework without pairing, the present paper describes the mechanisms leading to a generation of angular momentum at and after the scission as a function of the orientation of the two fragments with the fission axis and their relative azimuthal angle. With the FHF method, the potential at and after scission is obtained as a function of the orientations of the fragments exploring two fission modes of ^{240}Pu fission with different shapes of the fragments. The TDHF calculation reveals how much angular momentum is generated in the fragments as a function of the initial orientation and how it is shared between collective rotation and noncollective orbital contributions.

The main conclusions are

- (1) the Coulomb potential at large distances creates a mainly collective rotation of the fragments while the nuclear interaction tends to generate more complex rotations, which are less collective;
- (2) an initial spherical nucleus such as the ^{132}Sn can rotate while remaining quasispherical with a noticeably purely noncollective angular momentum;
- (3) the noncollective angular momentum is seen to be transferred between the protons and the neutrons;
- (4) the generated angular momentum by the Coulomb force depends more on the deformation of the fragments than on the $Z_1 Z_2$ product. This result contradicts the argument of Ref. [36] against the postscission generation of angular momentum;
- (5) when both fragments are deformed the azimuthal angle does not play a role in the Coulomb-induced rotation and has a weak effect on the nuclear interaction producing a twisting mode.

ACKNOWLEDGMENTS

I want to thank A. Bulgac and G. Bertsch for interesting and fruitful discussions and for carefully read the manuscript. The funding from the US DOE, Office of Science, Grant No. DE-FG02-97ER41014 is greatly appreciated. This research used resources of the Oak Ridge Leadership Computing Facility, which is a U.S. DOE Office of Science User Facility supported under Contract No. DE-AC05-00OR22725.

APPENDIX: GRAM-SCHMIDT ORTHOGONALIZATION

In Fig. 10, the effect of the orthogonalization on the rotational potential is shown. It can be seen that the Gram-Schmidt procedure change strongly the shape of the potential which becomes incompatible with the dynamical results presenting a strong torque for θ_H close to zero. This result confirms the statement of Ref. [19] that the Gram-Schmidt should not be used with the FHF method.

- [1] L. G. Moretto and R. P. Schmitt, *Phys. Rev. C* **21**, 204 (1980).
- [2] T. Døssing and J. Randrup, *Nucl. Phys. A* **433**, 215 (1985).
- [3] J. Randrup and R. Vogt, *Phys. Rev. Lett.* **127**, 062502 (2021).
- [4] J. Randrup, T. Døssing, and R. Vogt, *Phys. Rev. C* **106**, 014609 (2022).
- [5] I. N. Mikhailov and P. Quentin, *Phys. Lett. B* **462**, 7 (1999).
- [6] L. Bonneau, P. Quentin, and I. N. Mikhailov, *Phys. Rev. C* **75**, 064313 (2007).
- [7] S. Franke-Arnold, S. M. Barnett, J. Leach, J. Courtial, and M. Padgett, *New J. Phys.* **6**, 103 (2004).
- [8] M. M. Hoffman, *Phys. Rev.* **133**, B714 (1964).
- [9] K. Alder and A. Winther, *Electromagnetic Excitation: Theory of Coulomb Excitation with Heavy Ions* (North-Holland, Amsterdam, 1975).
- [10] G. F. Bertsch, [arXiv:1901.00928](https://arxiv.org/abs/1901.00928).
- [11] Ș. Mișicu, A. Săndulescu, G. M. Ter-Akopian, and W. Greiner, *Phys. Rev. C* **60**, 034613 (1999).
- [12] J. O. Rasmussen, W. Nörenberg, and H. J. Mang, *Nucl. Phys. A* **136**, 465 (1969).
- [13] G. F. Bertsch, T. Kawano, and L. M. Robledo, *Phys. Rev. C* **99**, 034603 (2019).
- [14] P. Marević, N. Schunck, J. Randrup, and R. Vogt, *Phys. Rev. C* **104**, L021601 (2021).
- [15] A. Bulgac, I. Abdurrahman, S. Jin, K. Godbey, N. Schunck, and I. Stetcu, *Phys. Rev. Lett.* **126**, 142502 (2021).
- [16] A. Bulgac, I. Abdurrahman, K. Godbey, and I. Stetcu, *Phys. Rev. Lett.* **128**, 022501 (2022).
- [17] A. Bulgac, S. Jin, and I. Stetcu, *Phys. Rev. C* **100**, 014615 (2019).
- [18] Y. Tanimura, D. Lacroix, and S. Ayik, *Phys. Rev. Lett.* **118**, 152501 (2017); **121**, 059902(E) (2018).

- [19] C. Simenel, A. S. Umar, K. Godbey, M. Dasgupta, and D. J. Hinde, *Phys. Rev. C* **95**, 031601(R) (2017).
- [20] A. S. Umar, C. Simenel, and K. Godbey, *Phys. Rev. C* **104**, 034619 (2021).
- [21] V. Y. Denisov and W. Nörenberg, *Eur. Phys. J. A* **15**, 375 (2002).
- [22] K. Washiyama and D. Lacroix, *Phys. Rev. C* **78**, 024610 (2008).
- [23] C. Simenel and B. Avez, *Int. J. Mod. Phys. E* **17**, 31 (2008).
- [24] C. Simenel, *Eur. Phys. J. A* **48**, 152 (2012).
- [25] P. A. M. Dirac, *Math. Proc. Cambridge Philos. Soc.* **26**, 376 (1930).
- [26] C. Simenel, D. Lacroix, and B. Avez, *Quantum Many-body Dynamics: Applications to Nuclear Reactions* (VDM Verlag, Sarrebruck, 2010).
- [27] K.-H. Kim, T. Otsuka, and P. Bonche, *J. Phys. G: Nucl. Part. Phys.* **23**, 1267 (1997).
- [28] S. Jin, K. J. Roche, I. Stetcu, I. Abdurrahman, and A. Bulgac, *Comput. Phys. Commun.* **269**, 108130 (2021).
- [29] B. Schuetrumpf, P.-G. Reinhard, P. D. Stevenson, A. S. Umar, and J. A. Maruhn, *Comput. Phys. Commun.* **229**, 211 (2018).
- [30] J.-F. Lemaître, S. Goriely, S. Hilaire, and J.-L. Sida, *Phys. Rev. C* **99**, 034612 (2019).
- [31] C. L. Zhang, B. Schuetrumpf, and W. Nazarewicz, *Phys. Rev. C* **94**, 064323 (2016).
- [32] G. Scamps and C. Simenel, *Nature (London)* **564**, 382 (2018).
- [33] A. Bulgac, S. Jin, K. J. Roche, N. Schunck, and I. Stetcu, *Phys. Rev. C* **100**, 034615 (2019).
- [34] Y. Qiang, J. C. Pei, and P. D. Stevenson, *Phys. Rev. C* **103**, L031304 (2021).
- [35] Z. X. Ren, D. Vretenar, T. Nikšić, P. W. Zhao, J. Zhao, and J. Meng, *Phys. Rev. Lett.* **128**, 172501 (2022).
- [36] J. N. Wilson, D. Thisse, M. Lebois *et al.*, *Nature (London)* **590**, 566 (2021).
- [37] A. Bulgac, *Phys. Rev. C* **106**, 014624 (2022).